Journal of Nanobiotechnology

RESEARCH Open Access

In situ and dynamic screening of extracellular vesicles as predictive biomarkers in immune-checkpoint inhibitor therapies

Yihe Wang[1], Yue Sun[1], Mengqi Liu[1], Chao Wang[1], Miao Huang[1], Jiaoyan Qiu[1], Ningkai Yang[1], Yu Zhang[1], Hong Liu[2] and Lin Han[1,3*]

Abstract

Extracellular vesicles (EVs) is promising in predicting the efficacy of immune checkpoint inhibitor (ICI) therapies. But it is challenging to determine the level of circulating EVs due to their variations in spatial and temporal distribution. To address this, we developed an in situ EV detection platform integrating multiplex EV capture with microfluidic-generated immune-tumor spheroids. This platform enables in situ monitoring of EV secretion dynamics under ICI and chemotherapeutic treatments, capturing localized and temporal changes in EV release. Using predictive models, we identified EVs carrying programmed cell death ligand 1 (PD-L1) as the most robust predictors of spheroid viability during treatment. RNA sequencing further revealed that dynamic EV expression changes are driven by gene transcription, providing a temporal understanding of EV regulation. Our platform overcomes the limitations of traditional methods by offering a physiologically relevant system to study EV-mediated immune responses. By addressing the spatial and temporal heterogeneity of EVs, this work advances EV-based biomarker discovery and provides a foundation for optimizing personalized immunotherapies.

Introduction

Immunotherapy is a critical method for cancer treatment, with immune checkpoint inhibitors (ICIs) designed to block checkpoint proteins, such as programmed cell death ligand 1 (PD-L1), cytotoxic T lymphocyte associate protein-4 (CTLA-4), and programmed death 1 (PD-1), from binding to their respective receptors, which otherwise suppress immune function [1]. While the efficacy of immunotherapy is comparable to traditional cancer treatments, it remains ineffective in many clinical cases [2]. To further enhance treatment efficacy and patient response rates, identifying more specific biomarkers and immune checkpoint inhibitors is essential [3–5]. This requires the development of more reliable predictive tools and assays for screening immunotherapy responders [6]. Effective biomarkers should enable the classification of patients and predict their response to specific immunotherapies [7]. Therefore, identifying suitable biomarkers to predict the efficacy of ICI therapies and improve immune checkpoint blockade outcomes remains a significant challenge in current immunotherapy research.

Extracellular vesicles (EVs) have been recognized as key players in several hallmarks of cancer, including angiogenesis, invasion, and metastasis [8–10]. Elevated levels of immune checkpoint proteins, such as PD-L1, expressed in the cancer-derived EVs have been shown to be potent mediators of immunosuppression [11–14]. In particular, the level of PD-L1 expressed on circulating exosomes (exocytosis EVs ranging from 40 to 160 nm

*Correspondence:
Lin Han
hanlin@sdu.edu.cn

Full list of author information is available at the end of the article

Graphic abstract

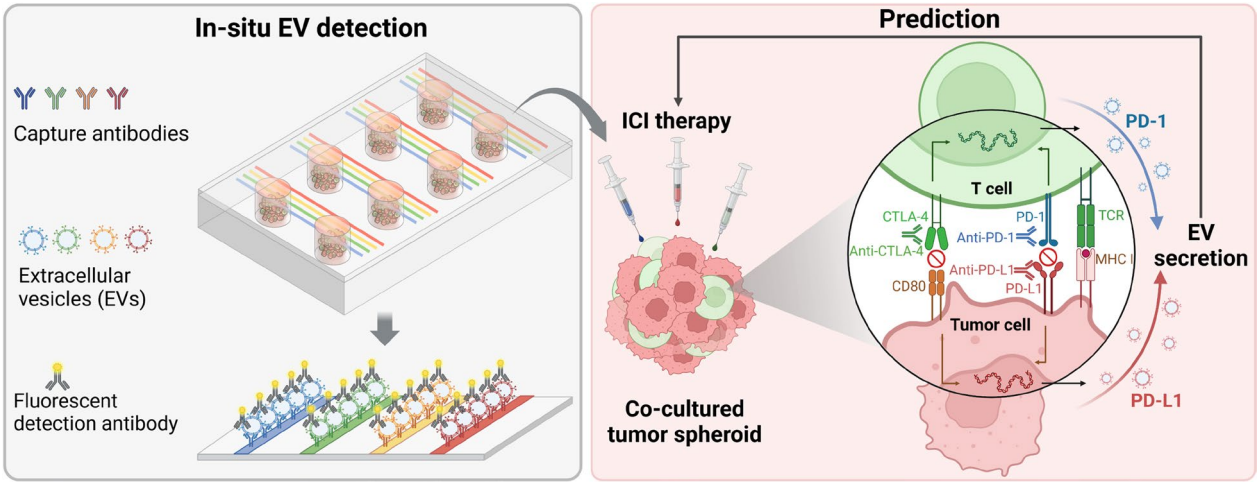

Highlights

- 1. In situ EV platform monitors dynamic secretion in tumor spheroids.
- 2. PD-L1 + EVs best predict ICI outcomes, driven by gene transcription.
- 3. This work integrates machine learning and RNA-seq for biomarker discovery.

Keywords Extracellular vesicles, Tumor spheroids, Immune checkpoint inhibitors, PD-L1, Machine learning

in diameter) [15] has been identified as an indicator of tumor cells' adaptive responses to T cells during the course of anti-PD-1 therapy in metastatic melanoma patients, thus allowing for the stratification of responders and non-responders to anti-PD-1 treatment [16]. These findings suggest that monitoring circulating exosomal PD-L1 could serve as a useful tool for predicting tumor responses to immunotherapy. Moreover, exosomal PD-L1 acts not only on tumor cells and the local tumor microenvironment but also on distal sites, such as secondary lymphoid organs, by targeting T lymphocytes [17]. It has also been observed that the expression of exosomal PD-L1 in the blood differs from that of cellular PD-L1 in local tumor biopsies, suggesting potential temporal and spatial variations in the distribution of exosomes carrying PD-L1 [12]. Therefore, the variation in the spatial and temporal distribution of circulating EVs represents a major challenge in the development of circulating EVs as reliable predictive biomarkers for ICI therapies.

In situ monitoring of EV dynamics provides a comprehensive approach to study EVs in both spatial and temporal dimensions. Intercellular and intracellular activities of EVs have been observed using high-resolution technologies, which help to elucidate mechanisms in various cellular processes [18–22]. While these studies have provided critical insights into EV activity in numerous cellular processes, they are often limited by the throughput of EV detection due to spectral overlap. The combination of multiplex EV detection with single-cell isolation has been used to detect EVs carrying different markers [23–26]. These methods have enabled the examination of EV secretion from tumor cells or tumor-immune cell pairs at the single-cell level. However, despite the fact that single-cell isolation can disentangle multiplex observations in an averaged cell population, it is still challenging to replicate the three-dimensional (3D) structure and complex components of the tumor microenvironment (TME). For example, incorporating immune cells into the 3D TME at a single-cell level is challenging, whereas immune cells, such as tumor-infiltrating lymphocytes, are a crucial criterion for the success of anti-PD-L1 and/or anti-PD-1-based immunotherapies [27]. 3D tumor spheroids generated through microfluidic techniques have been widely used as in-vitro models to mimic the TME and investigate cell-cell interactions [28, 29], stromal-to-cell effects [30, 31], and the evaluation of chemical [32–34] or photothermal treatments [35]. Notably, cytokines secreted from tumor spheroids can be captured and measured in situ using beads [36] or antibody-coated substrates [37, 38]. However, to the best of our knowledge, no studies have yet reported the in situ detection of EVs secreted from individual tumor spheroids.

Here, we developed a platform for in situ multiplex detection of EV secretion from spheroids formed by tumor and immune cells. The dynamic changes in the secretion of EVs carrying various biomarkers, such as the immunoregulatory molecules PD-1 and PD-L1, were examined as a function of drug treatment duration and

EV enrichment time. The predictive capacity of these EV biomarkers was validated by establishing several machine learning models based on the correlation between cell viability and EV secretion levels upon different drug treatments. Additionally, the transcriptome expression driving EV secretion in response to drug treatments were explored via RNA sequencing. Taken together, our work suggests that this in situ EV detection method, integrated with machine learning models and next-generation RNA sequencing, offers a promising platform for advancing the discovery of biomarkers for evaluating immune checkpoint therapies.

Materials and methods

Materials and cells

Roswell Park Memorial Institute (RPMI) 1640 medium and TrypLE were purchased from Gibco (Thermo Fisher Scientific, USA). Fetal bovine serum (FBS) was obtained from Cyagen Biosciences Inc. (China). Penicillin–streptomycin (PS) solution was purchased from Solarbio Science & Technology Co., Ltd. (China). MDA-MB-231 and Jurkat cells were obtained from Peking University Third Hospital and Shandong University Qilu Hospital, respectively. SU-8 3050 photoresist and developer were ordered from Bynano Co., Ltd. Polydimethylsiloxane (PDMS) and curing agent were obtained from Momentive Performance Materials Inc. (USA). Cell-laden droplets were generated from a fluorinated oil (Novec 7500, 3 M) containing 2% (w/w) FluoSurf surfactant (Emulseo, France). Graphene oxide quantum dots (GOQDs) were purchased from XFNANO Materials Tech Co., Ltd. (China). Bovine serum albumin (BSA) and 3-aminopropyltrimethoxysilane (APTES) were obtained from Sigma-Aldrich (USA). Phosphate-buffered saline (PBS) was acquired from Corning (USA). Capture antibodies against CD9, CD63, CD81, PD-1, PD-L1, IFN-γ, IL-1β, and IL-6, and biotin-labeled detection antibodies against IFN-γ, IL-1β, and IL-6 were ordered from R&D Systems (USA). Detection antibodies including Alexa Fluor® 594 anti-human CD63, FITC anti-human CD274 (B7-H1, PD-L1), and APC anti-human CD279 (PD-1), and Streptavidin-APC were purchased from BioLegend (USA). Alexa Fluor 488 E-Cadherin rabbit monoclonal antibody was purchased from Cell Signaling Technology. Ki-67 Monoclonal Antibody (FITC) and HIF-1α Monoclonal Antibody (APC) were purchased from eBioscience™ (USA). ActinRed, live-dead assay reagents, and trypsin were purchased from KeyGEN BioTECH (China). Cell Tracker Green and Cell Tracker Red were purchased from ThermoFisher (USA). Nivolumab (anti-PD-1), Pembrolizumab (anti-PD-1), Tremelimumab (anti-CTLA-4), Atezolizumab (anti-PD-L1), and Dacarbazine (NSC-45388) were purchased from Selleck (USA). Epirubicin was purchased from Pfizer (China). Sugemalimab was purchased from WuXi Biologics (China). Cadonilimab was purchased from Akeso Inc. (China). The CD3 and CD28 antibodies for T cell activation were purchased from Elabscience (China).

Microfluidic fabrication

The fabrication of masters and PDMS slabs for the microfluidic chip used in spheroid formation has been described in detail previously [38]. Briefly, the masters were fabricated by traditional photolithography, and the PDMS was prepared using soft-lithography. After hole punching at the inlets and outlets of the channel, the two PDMS slabs were physically bonded and sandwiched between two poly(methyl methacrylate) (PMMA) clamps to seal the device. For drug treatment of the spheroids, a PMMA slab with hollow chambers was placed on top of the spheroids. The master fabrication for preparing the antibody barcode slide was described in the Supporting Information.

Cell culture and T cell activation

MDA-MB-231 and Jurkat cells were cultured in RPMI 1640 medium supplemented with 10% FBS and 1% PS. For passaging MDA-MB-231 cells, the cells were detached from culture flasks (T25) by digestion with 2 mL of trypsin solution at 37 °C for 5 min, and the digestion was terminated by adding 3 mL of culture medium. The cell suspension was then centrifuged at 1200 rpm for 3 min, and the cells were resuspended in fresh medium. Jurkat cells were centrifuged at 1200 rpm for 3 min, then resuspended in T25 flasks at a density of 1×10^5 cells/mL, with the addition of 5 mL of culture medium. All cells were incubated in a cell culture incubator set at 37 °C with 5% CO_2. Cells were passaged every 2–3 days. Prior to introduction into the microfluidic chip, Jurkat T cells were activated with a mixture of CD3 and CD28 antibodies at a concentration of 4 μg/mL in the culture medium for one day. Afterward, the supernatant was discarded, and the remaining pellet was directly introduced into the microfluidic chip. For 2D cell culture, cells were seeded directly into a 96-well plate at 1×10^5 cells/well and cultured for the desired duration.

Formation and culture of spheroids

The formation of spheroids followed a similar method to those described previously [38]. In brief, the device was assembled after ultraviolet (UV) light sterilization of the PDMS and PMMA clamps for 30 min. Fluorinated oil powered by a pressure pump was injected into the channel to expel air bubbles. A cell suspension with a concentration of 1×10^6 cells/mL (MDA-MB-231 to Jurkat cell ratio of 1:1) was then introduced into the chip, replacing the fluorinated oil in the wells and channels. The cell suspension in the wells was emulsified into droplets by

fluorinated oil containing 2% surfactant. After disassembling the device, the microwell chip containing cell-laden droplets was immersed in culture medium to remove any residual oil. The cells in the microwells were subsequently cultured for 24 h to promote the formation of spheroids with tight intercellular connections. For drug treatments, spheroids in each row were exposed to 100 μL of drug/medium solution, with daily drug/medium changes.

Viability test

A solution of calcein-AM (0.02% w/w) and propidium iodide (PI) (0.02% w/w) in PBS was used to stain cells at room temperature for 30 min. Fluorescence images were acquired using a Nikon Ti2 fluorescence microscope. The cell viability in 2D and 3D formats was defined as the ratio of integrated green fluorescence to the total integrated fluorescence (green and red) in the fluorescence images after live/dead staining.

Immunofluorescent staining

Spheroids were fixed in 4% paraformaldehyde in PBS for 20 min and permeabilized at room temperature with 0.2% Triton X-100 for 5 min. Cells were then blocked with 3% BSA in PBS for 1 h. The first group of spheroids was stained with E-cadherin (1:200 dilution) and Actin-Red (1:50 dilution), the second group with Ki-67 (1:400 dilution) and HIF-1α (1:50 dilution), and the third group with PD-L1 (1:20 dilution) and PD-1 (1:20 dilution) at 4 °C overnight. After three washes with PBS, cell nuclei were stained with DAPI for 15 min, and the spheroids were sealed with a cover slide. The stained spheroids were imaged using a Zeiss LSM880 confocal microscope.

Preparation of antibody barcode slide

The glass slide for EV detection was pre-modified with capture antibodies. Briefly, following oxygen plasma treatment, the surfaces of the glass slides were functionalized with APTES and GOQDs. A 2 μL volume of antibody solution was then introduced into each microchannel and withdrawn using a vacuum pump for over 4 h until the antibodies were completely bound to the GOQDs on the glass surface. The design of the channels for immobilizing the capture antibodies is illustrated in Fig. **S1** (Supporting Information).

EV and cytokine detection

Before covering the detection glass slide, 1 mL of cell culture medium was loaded onto the microwells to wet the surface of the chip and prevent bubble formation. A lead block was placed on top of the slide to drain the liquid between the microwell and the slide, ensuring a seal. The entire setup was placed in a 37 °C incubator to maintain humidity for cell culture. Before imaging the captured EV slide, 400 μL of Alexa Fluor® 594 CD63 detection antibody (1:100 dilution in 1% BSA) was added to the barcode slide and incubated for 45 min. The glass slide was then rinsed with PBS and distilled water. For fluorescence imaging, the slide was scanned using a GenePix 4400 A scanner with a 594 nm laser at 100% power and 600 PMT gain. Images from the scanner were analyzed using GenePix Pro software. The detection of captured cytokines on the slide followed the same protocol as EV detection, with modifications in the detection system. Biotin-labeled detection antibodies (diluted 1:100 in 1% BSA) were used, followed by APC-conjugated streptavidin (1:100 dilution in 1% BSA, 30-minute incubation) for fluorescent labeling. Imaging was performed using a 635 nm laser at 80% power and a PMT gain of 500. For cytokine detection in 2D cultured cell suspensions, a PDMS slab containing rectangular wells (2 mm in length) was bonded to the antibody-barcode slide to create sample-loading chambers. Each cell suspension sample (4 μL) was loaded into the designated wells and incubated for 45 min to allow cytokine capture on the slide.

SEM imaging

Prior to imaging, the EVs bound to the barcode glass slide were coated with Pt nanoparticles using a Hitachi MC1000 Ion Sputter Coater for 20 s at 15 mA. Imaging was conducted on a Scanning Electron Microscope (HITACHI UHR FE-SEM SU8200 Series).

Machine learning

The correlation between cell viability and the EV secretion change factor under different drug concentrations was established using a linear regression model, a nonlinear regression model, and a logistic regression model with JMP Pro. In the linear regression model, the parameters for each independent variable were estimated using a least squares estimator. Nonlinear regression analysis was performed using the Neural Network function in JMP Pro, with a one-layer feed-forward neural network and a hyperbolic tangent function with 10 hidden neurons. In the logistic regression model, cell viability was classified into two categories: 1 (0.7-1.0) and 2 (0-0.7). The ROC curve was plotted by evaluating the changes in the positive rate (Sensitivity) against the false positive rate (1-Specificity) for different cut-offs of EV secretion and drug treatment conditions. For all three regression models, 75% of the data were used for training the algorithm, and 25% were used to independently test the models.

RNA-seq and analysis

The spheroids in each row of microwells were first dissociated into individual cells by enzymatic digestion with 100 μL of TrypLE for 10 min, followed by physical agitation. The collected cells were then lysed for RNA

extraction using a kit (Quick-RNA Microprep Kit, Zymo Research). The RNA quality was checked using an Agilent 2100 Bioanalyzer. The purified RNA was indexed using the TruSeq RNA sample preparation kit and sequenced on the Novaseq PE150 platform (Illumina). For data analysis, HISAT2 was used to align reads to the latest Ensembl release 47 human genome/transcriptome (GRCh38.p14). Samtools was used to generate raw counts from alignment files (SAM). Differentially expressed genes, Principal Component Analysis (PCA), and Kyoto Encyclopedia of Genes and Genomes (KEGG) pathway analysis were performed using the NovoMagic online tool.

Statistical analysis

All experiments were performed in triplicate ($n = 3$) to assess reproducibility. Statistical analysis was conducted using Origin. A t-test was employed to evaluate the significance of differences in cell viability between the 2D and 3D models. One-way ANOVA was used to assess the statistical significance of differential effects under various conditions on cell viability and EV secretion, with the significance threshold set at $p \leq 0.05$.

Results and discussion

A co-cultured tumor spheroid model for in situ and dynamic detection of extracellular vesicles after immune-checkpoint inhibitor treatments

Immunotherapy includes immune checkpoint inhibitors (ICIs) designed to block checkpoint proteins, such as PD-L1 and PD-1, as depicted in Fig. 1A. The in situ detection of extracellular vesicles (EVs) is used to assess the efficacy of immunotherapy, serving as more specific biomarkers. In this study, "in situ" specifically denotes a localized EV detection method that analyzes EVs within their original 3D spheroid microenvironment, without physical disruption or isolation. Tumor spheroids, formed from a mixture of tumor cells and T cells, were generated using a self-digitization method [38, 39]. Briefly, a microfluidic chip composed of two polydimethylsiloxane (PDMS) slabs—one containing a serpentine channel and the other an array of microwells—was used to create tumor spheroids (Fig. 1B). The mixture of tumor cells and T cells was introduced into the microwells after air was expelled by a flow of fluorinated oil. Subsequently, fluorinated oil was reintroduced to shear the cell suspension in the microwells into droplets. Finally, the oil was replaced with cell culture medium for long-term culture. Using this method, an array of hundreds of cell-laden droplets was generated within the microfluidic chip. Figure 1C illustrates the workflow for ICI treatments and in situ EV detection on co-cultured spheroids. After one day of culture, the tumor cells and T cells in the droplets assembled into spheroids through intercellular connections. Drug solutions were then added to each row of spheroids for treatments of varying durations (2–7 days). A glass slide functionalized with stripes of capture antibodies, referred to as barcode antibodies, was placed perpendicular to the rows of spheroids to capture and detect the secreted EVs with an enrichment of 8–24 h. Eventually, the drug-treated spheroids in each row were dissociated into individual cells for subsequent RNA sequencing. The captured EVs from individual spheroids on the functionalized slide were detected using a fluorescently labeled CD63 detection antibody (Fig. 1D). This method enabled the determination of EV secretion levels from a single spheroid based on the fluorescent intensity of the detection antibodies immobilized on the barcode antibodies.

The captured EVs for individual spheroids appeared as a barcode stripe pattern on the slide, as shown in Fig. 1E. This approach enabled the detection of multiple EVs from hundreds of individual spheroids subjected to varying drug treatments on a single slide. By adjusting the drug treatment or EV enrichment time, we could obtain changes in EV secretion by comparing treated samples with the untreated control group. Statistical correlations were established between spheroid viability and changes in EV secretion, enabling the prediction of the viability of unknown samples for the evaluation of ICI therapies. The treated spheroids were also recovered and lysed for subsequent investigation of genomic mechanisms involved in immune pathways and gene expression.

Immune-check point expression in the co-cultured spheroids

The spheroids generated through this self-digitization method exhibited a high degree of uniformity in both size and cell viability. MDA-MB-231 breast cancer cells and activated Jurkat T cells, used in a 1:1 ratio, were employed to establish the co-cultured spheroids as a model for tumor and immune cells, respectively. The 50% ratio of Jurkat T cells in the spheroids represents the leukocyte infiltration can account for up to 50% of cellular composition in some cancer types [40–42]. As a proof-of-concept study, we employed two standardized cell lines (MDA-MB-231 and Jurkat) to establish a controlled experimental system. The use of well-characterized lines provided a reproducible platform to isolate and validate the specific contributions of EVs, forming a critical foundation for future translational studies. Previous studies have demonstrated the secretion of exosomal PD-L1 by MDA-MB-231 cells and the secretion of exosomal PD-1 by activated Jurkat cells [43–45]. Figure 2A shows a bright-field image of the spheroids following one day of culture on the chip. The spheroid diameter exhibited high uniformity, with a coefficient of variation (CV) consistently below 0.5% across all replicates, as demonstrated

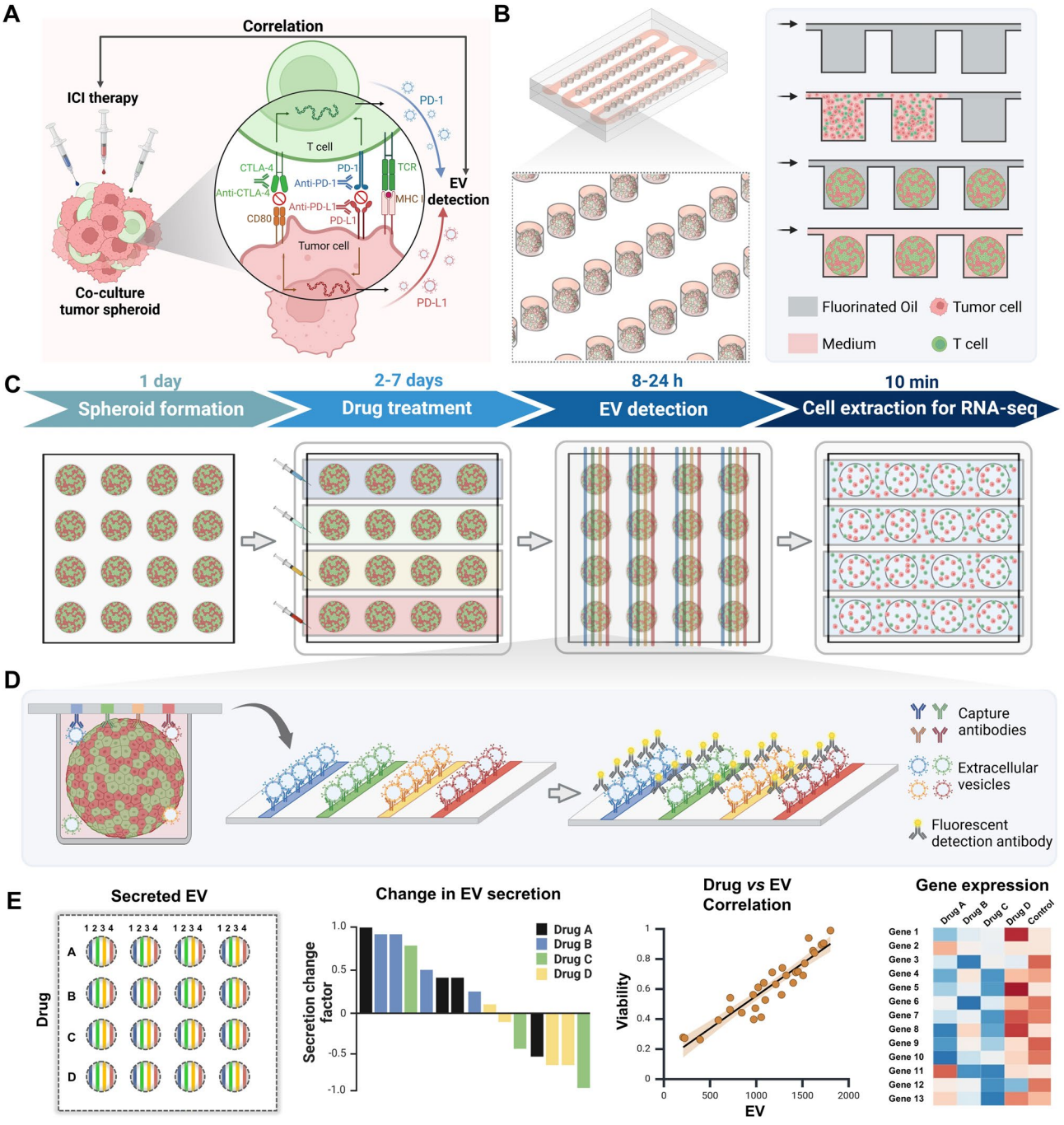

Fig. 1 Schematics of the formation of multicellular tumor spheroids, drug treatment, and extracellular vesicle (EV) detection. (**A**) Overview of the work principle. (**B**) Schematic of the microfluidic generation of co-cultured spheroids. (**C**) Workflow of the spheroid formation, drug treatment, in-site EV detection, and cell extraction for RNA sequencing. (**D**) Principle for EV detection using a barcode slide. (**E**) The main output results of this work

by the size distribution histograms in Fig. S2 (Supporting Information). Additionally, spheroid formation efficiency reached nearly 100% in all 216 microwells per chip, ensuring reliable and reproducible 3D cell culture production. After staining with Cell-Tracker Green and Cell-Tracker Red, the viable MDA-MB-231 cells and Jurkat T cells within the spheroids are distinctly visible, as shown in Fig. 2B. The merged fluorescent image of green MDA-MB-231 cells and red Jurkat T cells in Fig. 2C further confirms the co-existence of both cell types.

To verify the formation of tumor spheroids, the cells were stained in the co-cultured spheroid after one day of culture with E-cadherin, a cell surface marker for intercellular connections [46, 47] (Fig. 2D). The cytoskeletons

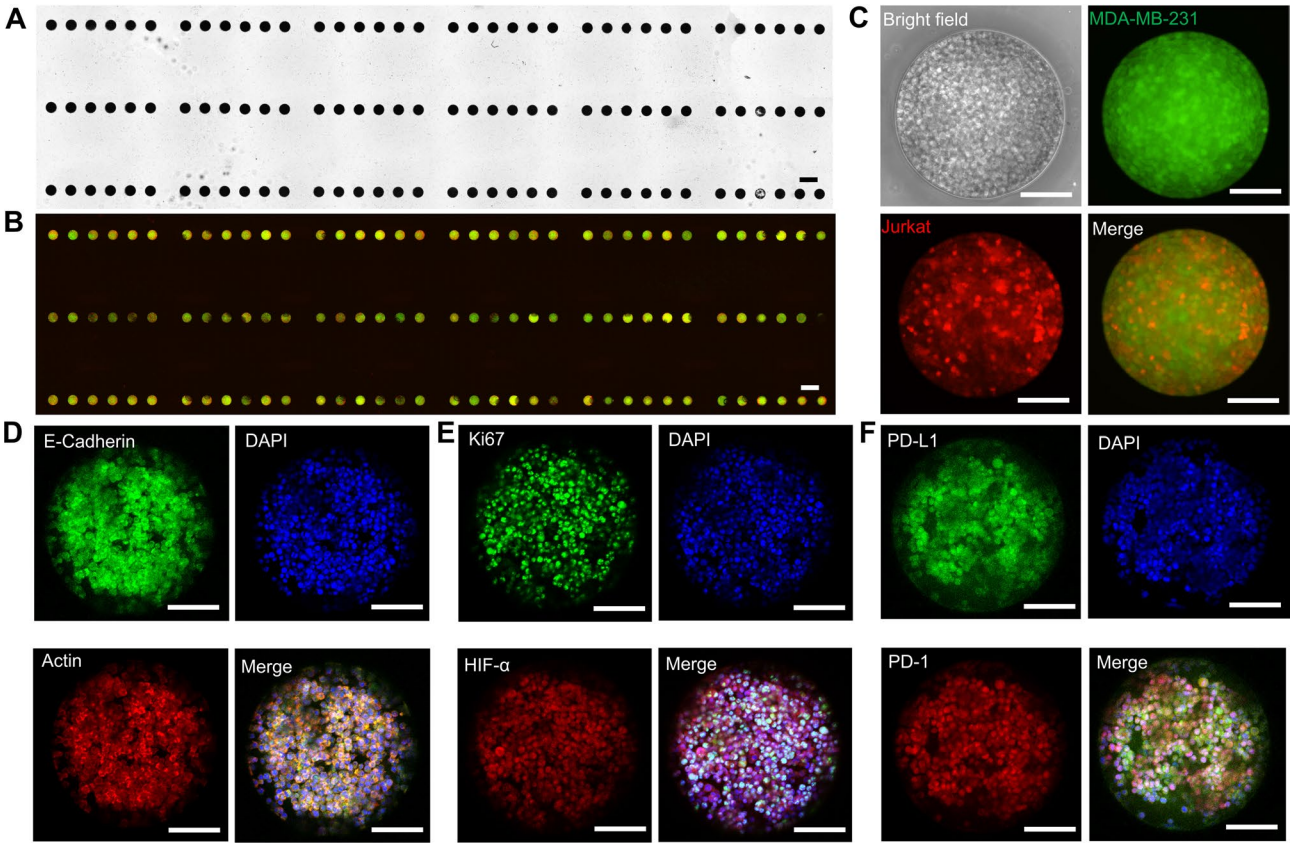

Fig. 2 Morphological characterization of spheroids from MDA-MB-231 breast cancer cells and Jurkat T cells. (**A**) Bright-field image of a representative portion of the spheroids formed from MDA-MB-231 and Jurkat cells using the microfluidic platform. Scale bar = 500 µm. (**B**) Fluorescence images of co-cultured spheroids stained with Cell-Tracker Green for viable MDA-MB-231 cells and Cell-Tracker Red for viable Jurkat cells after one day of culture. Scale bar = 500 µm. (**C**) Bright-field and fluorescence images of the co-cultured spheroid stained with Cell-Tracker dyes. Scale bars = 100 µm. Immunofluorescence staining of spheroids after one-day culture: (**D**) E-cadherin (green) and Actin-Red (red); (**E**) Ki67 (green) and HIF-1α (red); (**F**) PD-L1 (green) and PD-1 (red), and DAPI (nuclei, blue), with merged fluorescence images for D, E, and F. Scale bars = 100 µm for D, E, and F

and nuclei of the cells were stained with Actin-Red and DAPI, respectively. The expression of Ki67 and HIF-1α indicates the cell proliferation and hypoxic state of the spheroids, respectively (Fig. 2E). The expression of cellular PD-L1 and PD-1 was confirmed by immunofluorescent staining of PD-L1 and PD-1 on the cell surface, as shown in Fig. 2F.

Cytotoxicity of ICIs to the co-cultured 3D spheroids and traditional 96-well plate based 2D cultured cells

To validate the co-cultured model in the evaluation of ICI treatments, we selected Atezolizumab, Nivolumab, and Tremelimumab as model drugs for anti-PD-L1, anti-PD-1, and anti-CTLA-4 therapies, respectively. For comparison, Epirubicin was chosen as a chemotherapeutic drug. The concentration of ICIs was set at 1×10^2 mg/mL to be comparable with that used in clinical ICI treatments. Epirubicin was applied at varying concentrations to the co-cultured cells in both 3D and 2D cultures.

Figure 3A presents images of MDA-MB-231 and Jurkat cells in 2D culture using a fluorescent live-dead assay after two days of various drug treatments. The green and red fluorescence in the cells identifies viable and dead cells, respectively. The tumor cells and T cells under ICI treatments show higher cell density and viability compared to those under chemotherapeutic treatments. Figure 3B shows the live-dead staining of co-cultured 3D spheroids after two days of drug treatment, with varying drug types (Fig. 3B, left panel) and varying concentrations of Epirubicin (Fig. 3B, right panel). Tumor spheroids in 3D format better mimic the TME in a more physiological condition compared to 2D monolayer cell cultures. To compare cell activity in 2D and 3D formats, the cellular viability is summarized in both culture formats after two days of drug treatments at a concentration of 1×10^2 mg/mL (Fig. 3C). Cell viability in 3D format was lower than that in 2D format for ICI treatments, while remaining similar for chemotherapeutic treatments. This may be due to the restricted space for tumor growth and higher tumor-T cell interactions in 3D format compared to the 2D format. Moreover, the viability of cells treated with ICIs was higher than that of cells treated with chemotherapeutic

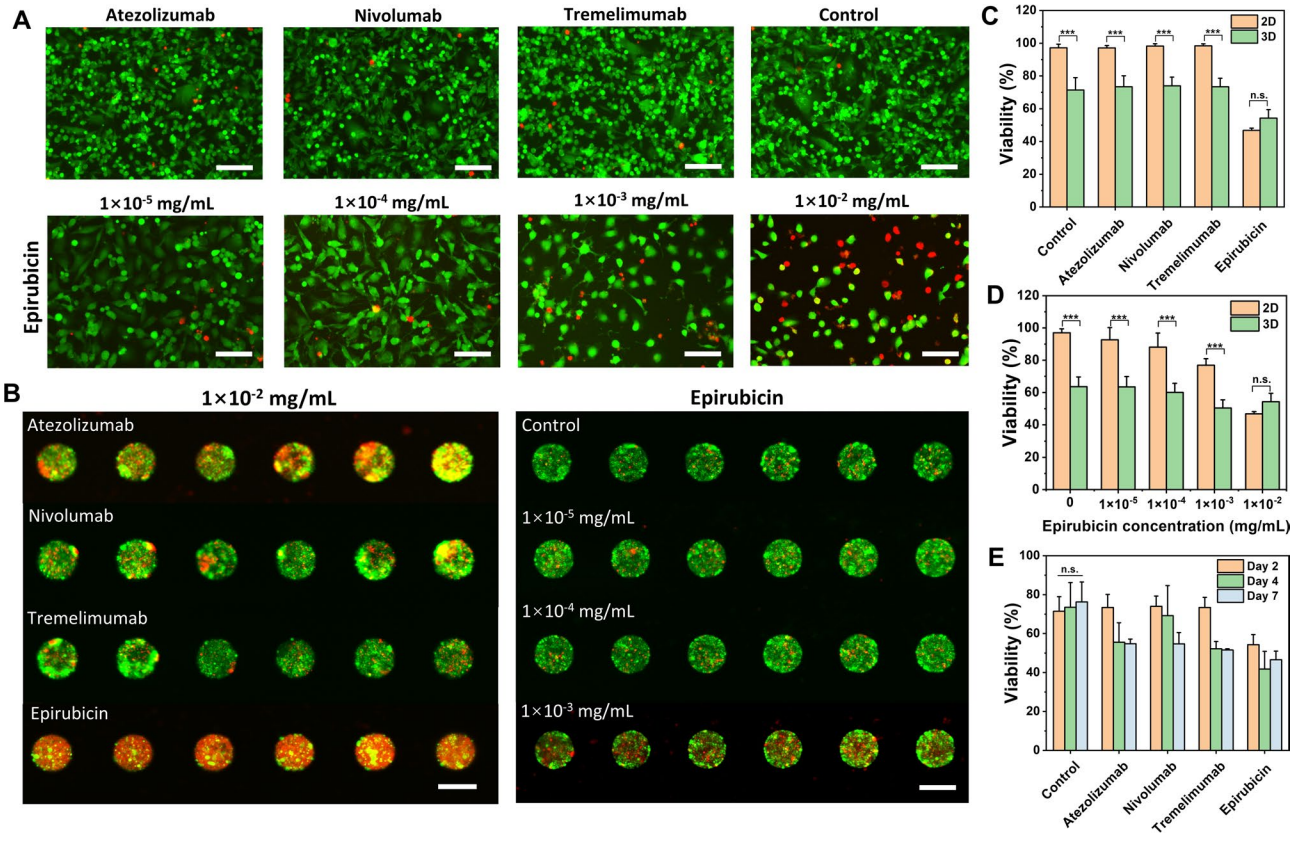

Fig. 3 Viability of MDA-MB-231 and Jurkat cells in 3D and 2D models after drug treatments. **A**. Fluorescence microscopy images of co-cultured cells stained with a Live/Dead assay after two days of drug treatments for Atezolizumab, Nivolumab, Tremelimumab, and Epirubicin at 1×10^{-2} mg/mL and for Epirubicin at 0, 1×10^{-5}, 1×10^{-4}, 1×10^{-3}, and 1×10^{-2} mg/mL in 2D (**A**) and 3D (**B**) formats. Scale bars in A = 100 µm, and in B = 300 µm. **C**. Viability of MDA-MB-231 and Jurkat cells in 3D and 2D models for two-day drug treatments at 1×10^{-2} mg/mL. Data were analyzed from 60 spheroids and triplicates in 96-well plates for 3D and 2D models, respectively. **D**. Viability of MDA-MB-231 and Jurkat cells in 3D and 2D models for two-day drug treatment of Epirubicin at 0, 1×10^{-5}, 1×10^{-4}, 1×10^{-3}, and 1×10^{-2} mg/mL. E. Viability of cells in 3D spheroids for drug treatments at 2, 4, and 7 days. Data are presented as the mean ± standard deviation. Statistical significance was determined using Student's t-test: n.s. for $p > 0.05$, *$p < 0.05$, **$p < 0.01$, ***$p < 0.001$. One-way ANOVA test for viability grouped by the same drug in panel E: $p > 0.05$ for n.s. and $p < 0.05$ for unmarked data

drugs at the same concentration in both 2D and 3D models. Figure 3D shows that cell viability decreased as the concentration of Epirubicin increased in both 2D and 3D formats, with viability being higher in the 2D culture format than in the 3D format.

Cell viability at different treatment times was also investigated. Figure 3E shows changes in cell viability in 3D co-cultured spheroids at 2, 4, and 7 days. Cell viability began to significantly decrease by day 4 for treatment of Atezolizumab and Tremelimumab, and by day 7 for treatment of Nivolumab. In contrast, cells treated with Epirubicin showed a dramatic decrease in viability at day 2 and only slight decreases at day 4 and day 7, indicating a faster cellular response to chemotherapeutic treatment than to ICI treatments. The live-dead staining and cellular viability in 2D culture at different treatment times are presented in Fig. S3 (Supporting Information). Our results reveal a pronounced reduction in cell viability within the 3D spheroid co-culture system following prolonged ICI treatment (2–7 days). In contrast, 2D monolayer cultures maintained consistently high viability throughout the treatment period (Fig. S3B, Supporting Information). This differential response may stem from potential activation-induced phenotypic changes in Jurkat cells under extended 3D co-culture conditions, and the enhanced cell-cell interactions intrinsic to the 3D spheroid architecture, which likely promote immune synapse formation and amplify cytotoxic effects. Furthermore, the high viability of MDA-MB-231 cells in 2D monolayer cultures treated with the same ICIs suggests minimal cytotoxicity of ICIs toward these cells (Fig. S4, Supporting Information).

To evaluate immune-mediated cytotoxicity, we quantified key cytokines (IFN-γ, IL-1β, and IL-6) in 3D co-culture spheroids and 2D culture supernatants after 2, 4, and 7 days of treatment with Atezolizumab, Nivolumab, Tremelimumab, or Epirubicin. The concentration of the cytokines was represented from the fluorescence intensity of the captured cytokines labeled with the fluorescence detection antibodies (Fig. S5A, supporting

information). As expected, IFN-γ was undetectable in both culture systems, consistent with reports that Jurkat T cells only produce IFN-γ upon phorbol myristate acetate (PMA)/ionomycin stimulation [48, 49]. In contrast, IL-6 was elevated in both 3D and 2D cultures, while IL-1β was specifically upregulated in 3D spheroids (Fig. S5, supporting information). Cytokine secretion (IL-6 and IL-1β) declined over time with prolonged drug exposure. Notably, Atezolizumab treatment significantly increased both IL-6 and IL-1β levels compared to untreated controls, suggesting a pro-inflammatory response. Conversely, Tremelimumab reduced secretion of these cytokines, implicating an anti-inflammatory role. In contrast, cytokine secretion was dramatically reduced in both 3D and 2D cultured cells upon Epirubicin treatment, highlighting the drug's nonspecific cytotoxicity toward immune and tumor cells.

Dynamic secretion of extracellular vesicles and its predictive validity of cell viability for ICI treatments

To investigate the predictive capability of EVs in evaluating ICI treatments, we developed a method to establish a correlation between the secreted EVs and the viability of co-cultured spheroids in response to drug treatments. The EVs secreted from individual co-cultured spheroids were captured by various antibodies (CD9, CD63, CD81, PD-1, and PD-L1) immobilized on a glass slide functionalized with graphene oxide quantum dots (GOQDs), as previously reported [50–52]. The GOQDs on the glass were used to immobilize the antibodies and minimize background noise from the fluorescent signals. Various capture antibodies were introduced through a set of parallel microchannels (20 μm in width and 30 μm in depth) above the GOQD-modified glass slide, where they were adsorbed, forming barcode-like antibody stripes. The design of the microfluidic channels for antibody immobilization and the uniformity of antibody capture on the slide were demonstrated in Fig. **S1** (Supporting Information). A fluorescent IgG solution was incubated to interact with the capture antibodies immobilized on the glass slide, thereby enabling the quantification of their density. The relative standard deviation (RSD) of IgG fluorescence intensity for all capture antibodies was below 15%. This method facilitates the application of multiple capture antibodies above individual spheroids, enabling the simultaneous detection of multiple types of EVs from a single spheroid.

A fluorescently labeled antibody (CD63), a typical membrane protein on EVs [22], was incubated to bind to the captured EVs on the slide, allowing quantification of EVs based on the fluorescence intensity of CD63. Figure 4A shows the fluorescence pattern of the detection antibodies conjugated on EVs secreted from individual spheroids. To verify the capture of EVs on the barcode glass slide, the slide was imaged using scanning electron microscopy (SEM), as shown in Fig. 4B. The EVs captured on the barcode glass slide exhibited a size distribution primarily in the range of 90–400 nm in diameter, with 52% of EVs in the range < 200 nm, categorized as small extracellular vesicles (sEVs) [53]. To confirm that serum-derived EVs do not interfere with our detection, we compared EVs isolated from spheroid-containing microwells with those from cell-free microwells (Fig. S6, Supporting Information). The results demonstrate that serum EVs have negligible background effects on the detection of spheroid-secreted EVs.

To explore the temporal changes in EV secretion for individual spheroids, the EV quantity was examined for an enrichment time of 8, 16, and 24 h after two days of drug treatments. The statistical distribution of fluorescent intensity for EVs (captured by CD9, CD63, CD81, PD-1, and PD-L1 antibodies) from treatments with four drugs and the non-treated control condition is plotted in Fig. 4C (left scale). To normalize EV secretion levels, we defined a secretion change factor as the ratio between the difference in average fluorescence intensity for treated and untreated spheroids and that for untreated spheroids. The variation in secretion change factor of co-cultured spheroids treated with four drugs at different EV enrichment times is shown in Fig. 4C (right scale). A positive value of the secretion change factor indicates increased EV secretion, while a negative value indicates decreased secretion. For CD63-expressed EVs, the secretion change factor significantly increased as the EV enrichment time increased from 8 h to 24 h for all four drugs. The average fluorescent intensity and the secretion change factor of EVs secreted from the spheroids treated with different drug conditions for various treatment and enrichment durations were presented in Table **S1** and S2 (supporting information), respectively. The duration of drug treatment is another factor influencing EV secretion levels. Drug treatment times of 2, 4, and 7 days were applied to co-cultured spheroids for EV enrichment of 16 h. Figure 4D (left scale) shows the statistical distribution of fluorescent intensity for the detected EVs after drug treatments of varying durations for four drugs and the control condition. The secretion change factor of co-cultured spheroids for different drug treatment times is plotted in Fig. 4D (right scale). The secretion change factor of PD-L1-expressing EVs decreased as the drug treatment time increased for all four drugs.

To explore the ability of EV secretion to predict cell viability, several machine learning models were established, including linear regression, non-linear regression, and logistic regression, for our co-cultured spheroid model using four types of drugs. The secretion change factor of EVs expressing CD9, CD63, CD81, PD-1, and PD-L1, the drug type, and the drug treatment time were defined

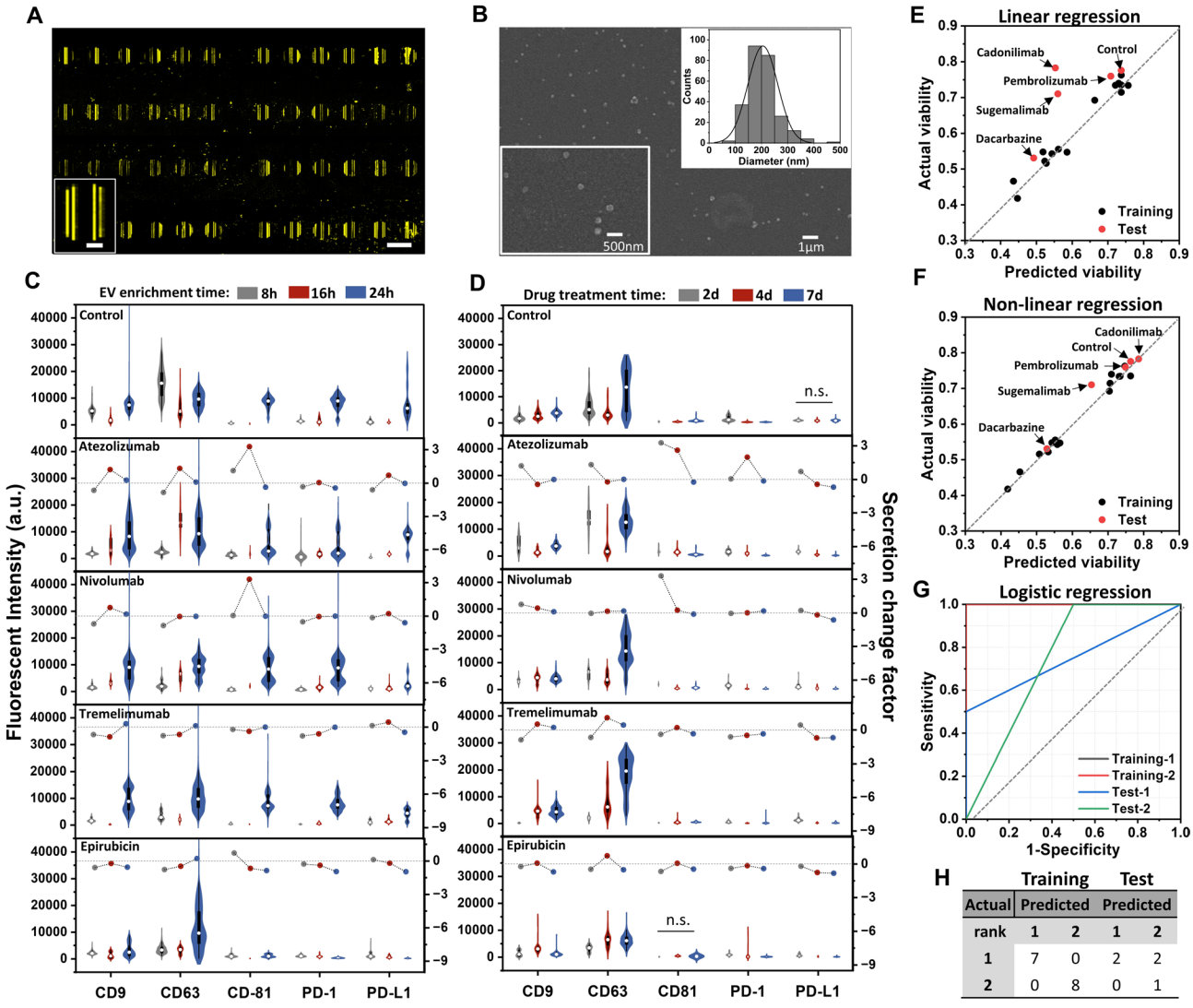

Actual	Training Predicted		Test Predicted	
rank	1	2	1	2
1	7	0	2	2
2	0	8	0	1

Fig. 4 Secretion change of EVs and its capability in predicting cell viability in this platform. (**A**) Representative fluorescence images of the secreted EVs captured and detected on a 2D functionalized glass slide for individual spheroids. The scale bars represent 300 μm for the larger image and 100 μm for the inset images. (**B**) Scanning electron microscopy (SEM) images of the EVs captured by the barcode slide, alongside the EV size distribution. **C**, **D**: Fluorescent intensity (left scale) and secretion change factors (right scale) of the EVs carrying CD9, CD63, CD81, PD-1, and PD-L1 secreted from co-cultured spheroids under the drug treatments with Atezolizumab, Nivolumab, Tremelimumab, Epirubicin (1×10^{-2} mg/mL) and control conditions. Data are shown for different EV enrichment times in C and different drug treatment durations in **D**. **E**, **F**: The actual viability plotted against the predicted viability of the spheroids for the training set and test set using a linear regression algorithm (**E**) and a non-linear regression algorithm (**F**). The training set was derived from the average viability of spheroids under drug treatments of Atezolizumab, Nivolumab, Tremelimumab, Epirubicin, and control condition over 2, 4, and 7 days. The test set was based on the average viability of spheroids under drug treatments with Sugemalimab, Pembrolizumab, Cadonilimab, Dacarbazine, and control conditions for 4 days. **G**. Receiver operating characteristic (ROC) curves obtained using a logistic regression algorithm to classify cell viability into two categories: 1 (0.7-1.0) and 2 (0-0.7). **H**. Confusion matrix for the training and test sets analyzed by the logistic regression model shown in **G**

as independent variables, and the viability of co-cultured spheroids was defined as the dependent variable. To validate our machine learning models for predicting untrained datasets, several drugs different than the ones in the training set were selected in the test set. The spheroids treated with Atezolizumab (anti-PD-L1), Nivolumab (anti-PD-1), Tremelimumab (anti-CTLA-4), Epirubicin (chemotherapeutic drug), and control were used as the training group, and the spheroids treated with Sugemalimab (anti-PD-L1), Pembrolizumab (anti-PD-1), Cadonilimab (anti-CTLA-4), Dacarbazine (chemotherapeutic drug), and control were used as the test set. The secretion change factors and cell viability for the spheroids in the test set are shown in Fig. S7 (Supporting Information).

Figure 4E shows the actual viability of spheroids plotted against predicted viability for the training and test sets using a linear regression model. The gray dotted line

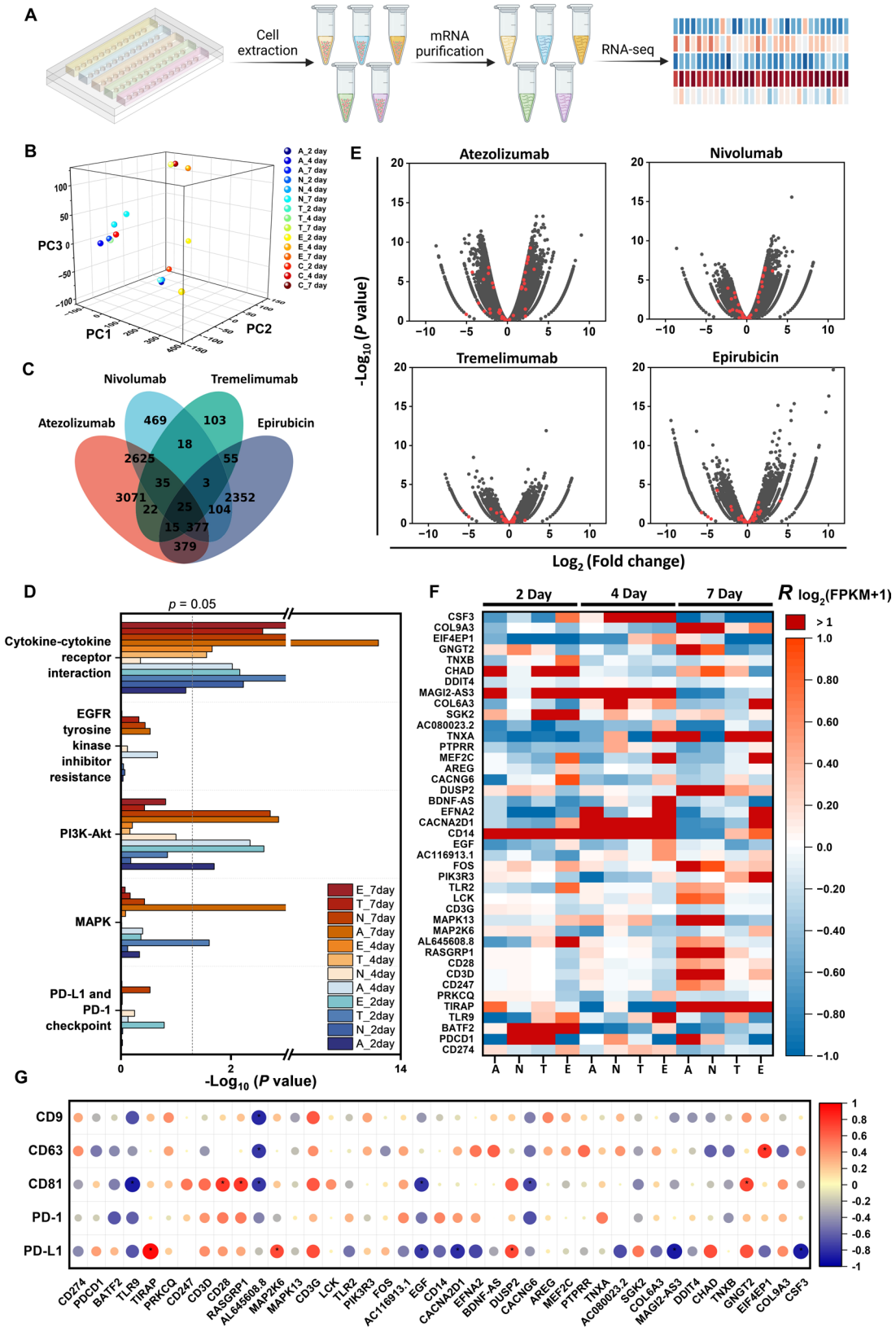

Fig. 5 (See legend on next page.)

(See figure on previous page.)

Fig. 5 RNA sequencing and differential gene expression analysis of the spheroids under different drug treatment conditions. (**A**) Schematic of cell isolation from the chip, mRNA purification, and RNA sequencing process used in the study. (**B**) The principle component analysis (PCA) of sequencing data from spheroids under treatment of Atezolizumab (**A**), Nivolumab (N), Tremelimumab (T), and Epirubicin (E), and non-treatment control (**C**) for 2, 4, and 7 days. (**C**) Venn diagram of differentially expressed genes among all groups for 7-day drug treatments. RNA sequencing and differential gene expression analysis revealed enrichment of 6549, 3656, 276, and 3310 genes for the treatment of Atezolizumab, Nivolumab, Tremelimumab, and Epirubicin, respectively, compared to the control group. (**D**) KEGG pathway clustering revealed differential presence of immune-related pathways among groups relative to the control group for different treatment conditions. (**E**) Volcano plots showing differentially expressed genes for all 7-day drug treatment groups relative to the control group (black dots). Red dots signify genes in immune-related pathways in D. (**F**) Heatmap showing expression of genes normalized as $R\ \log_2(FPKM+1)$ belonging to the pathways depicted in D. (**G**) Correlations between secretion change factor of EVs and expression levels of genes ($R\ \log_2(FPKM+1)$). The color and size of the circles indicate the value of Kendall's correlation coefficient. $^*p<0.05$

represents data where actual viability equals predicted viability. Each treatment condition for data points in the test set is annotated in Fig. 4E. It is found that when only the secretion change factor of PD-L1-expressing EVs and drug type were selected as independent variables, the coefficient of determination (R^2) reached 0.9633 with $p<0.05$ for both variables. The weights of each independent variable were estimated using a least square estimator. The estimated parameters and standard errors for each term are listed in Table S3 (Supporting Information), and the parameter for the secretion change factor of EVs carrying PD-L1 was the largest among all parameters. Therefore, the secretion change of PD-L1-expressing EVs is the optimal predictive factor for the treatment outcome of ICI and chemotherapeutic drugs in the linear regression model. Furthermore, the positive sign of the parameter associated with PD-L1 indicates a direct positive correlation between cell viability and the secretion change of PD-L1-expressing EVs. Cell viability was also predicted using a non-linear regression machine learning model with a hyperbolic tangent function and one hidden layer with 10 nodes. Figure 4F shows the actual cell viability plotted against predicted viability for the training and test sets using the non-linear regression model. The R^2 values for the training and test sets were 0.9839 and 0.9212, respectively, indicating better performance in predicting cell viability compared to the linear regression model. A logistic regression model was also applied to classify cell viability into two levels: 1 (0.7–1.0) and 2 (0–0.7). When only the secretion change factor of PD-L1-expressing EVs was defined as the independent variable, logistic regression showed optimal performance. The receiver operating characteristic (ROC) curves for the logistic regression model are shown in Fig. 4G. The ROC curve illustrates how the true positive rate (sensitivity) changes with the false positive rate (1 - specificity) for different cut-offs of the independent variable. The area under the curve (AUC) value indicates the model's ability to distinguish between the two categories of viability. The AUC for viability classification was 1 for the training set (training-1 and training-2) and 0.75 for the test set (test-1 and test-2). The confusion matrix obtained from the logistic regression analysis for the training and test sets is presented in Fig. 4H.

To summarize, cell viability in the untrained test set can be predicted based on the EV secretion change factor from the training set using a linear, non-linear, or logistic regression model. Although the non-linear regression model demonstrates the best predictive performance, it is challenging to assess the contribution of each variable to the overall prediction accuracy from the non-linear regression. In contrast, linear regression provides a direct evaluation of the contribution of each variable through the estimated parameters. Both linear and logistic regression analyses revealed that the secretion change of EVs carrying PD-L1 is the most significant contributor to predicting cell viability.

Temporal change of transcriptome expression for co-cultured spheroids under drug treatments

To explore the molecular mechanisms underlying the temporal changes in EV secretion after drug treatments, we performed RNA sequencing on cells from the co-cultured spheroids treated with Atezolizumab, Nivolumab, Tremelimumab, and Epirubicin, with no treatment as a control, for 2, 4, and 7 days. Figure 5A shows the workflow for sample preparation for RNA sequencing, starting from cell extraction from individual rows of spheroids under different treatment conditions. After cell lysis and mRNA purification, the sample solutions were prepared for RNA sequencing. Figure 5B presents the distribution of all samples along three dimensions based on their gene expression after Principal Component Analysis (PCA). The Venn diagram in Fig. 5C shows the differential gene expression for the four drugs compared to the control group after 7 days of treatment. The number of non-overlapping differentially expressed genes for spheroids treated with Atezolizumab, Nivolumab, Tremelimumab, and Epirubicin compared to the control condition was 3071, 469, 103, and 2352, respectively. The Venn diagram of the differential genes for the four drugs compared to the control group after 2-day and 4-day treatments is shown in Fig. S8A (Supporting Information). The correlations between different samples are plotted in Fig. S8B (Supporting Information).

To investigate the signaling pathways under different drug treatment conditions, we analyzed the RNA sequencing data via Kyoto Encyclopedia of Genes and

Genomes (KEGG) pathway clustering. We found that the pathways related to PD-1 and PD-L1 inhibition, including PD-1 and PD-L1 checkpoint (KEGG: 05235), MAPK (KEGG: 04010), PI3K-Akt (KEGG: 04151), EGFR tyrosine kinase inhibitor resistance (KEGG: 01521), and cytokine-cytokine receptor interaction (KEGG: 04060), were upregulated (Fig. 5D). The $-\log_{10}(P\text{value})$ of each sample indicates the activation significance of the aforementioned signaling pathways under different treatment conditions. Generally, samples treated for 7 days showed higher activation of these signaling pathways than those treated for 2 or 4 days. To visualize the regulation of the genes involved in these signaling pathways, we present volcano plots for all genes (black dots) and highlight the representative genes (red dots) involved in these pathways for the 7-day treatment samples in Fig. 5E. The volcano plots for the 2-day and 4-day treatments are presented in Fig. S8C (Supporting Information). The expression of the selected genes in these signaling pathways is shown in Fig. 5F. The expression of each gene was normalized using the $R\ \log_2(FPKM+1)$ method, which is defined as the ratio of the difference in $\log_2(FPKM+1)$ between drug-treated and control samples to the $\log_2(FPKM+1)$ of the control sample, where *FPKM* (Fragments Per Kilobase of transcript per Million mapped reads) is a normalization method for gene expression level. The *FPKM* values of these selected genes were listed in Table S4 (supporting information). The $R\ \log_2(\text{FPKM}+1)$ showed more pronounced changes for the 7-day treatment samples compared to the 2-day and 4-day treatment samples, suggesting increased activation of the signaling pathways regulating PD-1 and PD-L1 inhibition from 2 to 7 days of treatment. Specifically, the expression level of PD-L1 (CD274) decreased from day 2 to day 7, which is consistent with the trend observed in the secretion changes of EVs carrying PD-L1 (Fig. 4D).

Finally, to explore the correlation between gene expression and EV secretion, we calculated the correlation coefficients between the expression levels ($R\ \log_2(FPKM+1)$) of selected PD-1 and PD-L1-related genes and the secretion change factor of EVs across five surface markers (CD9, CD63, CD81, PD-1, and PD-L1) under different treatment conditions (Fig. 5G). Among the five markers, EVs carrying PD-L1 exhibited the greatest number of significant correlations with the selected genes, highlighting the importance of PD-L1 in the regulation of PD-1 and PD-L1-related gene expressions.

Conclusion

To address the spatial and temporal variations in the distribution of circulating extracellular vesicles (EVs) and identify effective biomarkers for immune checkpoint inhibitor (ICI) therapies, we developed an innovative platform for in situ detection of EVs secreted from individual co-cultured spheroids at multiple time points. This platform integrates a multiplex EV-detection barcode slide, enabling the quantification of EV secretion dynamics from single spheroids in response to various drug treatments. By combining this approach with machine learning models, we validated the predictive capacity of EVs in determining cellular viability under different treatment conditions.

Our platform is the first to enable in situ and dynamic monitoring of multi-EV secretion at the single spheroid level, capturing dynamic changes in EV secretion across both space and time. Using this system, we developed predictive models—including linear, non-linear, and logistic regression—based on correlations between cell viability and changes in EV secretion. Notably, changes in the secretion of PD-L1-expressing EVs showed the strongest correlation with cell viability under drug treatments, highlighting their potential as predictive biomarkers for assessing immunotherapeutic efficacy.

Further validation through RNA sequencing revealed that the expression of these EVs dynamically varies at specific time points of drug treatment, providing a temporal understanding of EV-mediated responses to treatment. This work not only advances the discovery of EV biomarkers for ICI therapies but also offers insights into novel strategies to overcome therapeutic resistance.

Our platform not only isolates specific EV contributions but also offers a scalable framework for transitioning to physiologically relevant systems. Future iterations incorporating patient-derived organoids will enable comprehensive evaluation of EV biomarkers across chemo-, targeted, and combination therapies, facilitating patient-specific response profiling. Furthermore, by integrating diverse immune cell populations (e.g., CD4+/CD8 + T cells, NK cells, macrophages, and Tregs) alongside multifaceted physicochemical gradients (such as hypoxia and nutrient deprivation), we can conduct mechanistic studies within complex tissue architectures—bridging the gap between foundational research and clinical translation. In addition, the low expression of CTLA-4 in Jurkat cells restricts our ability to evaluate the drug's direct interaction with its target receptor, including downstream checkpoint regulation (e.g., CD28 co-stimulation or PD-1 cross-talk). Future studies employing CTLA-4 + primary T cells or gene-edited Jurkat models would strengthen these findings.

Supplementary Information

The online version contains supplementary material available at https://doi.org/10.1186/s12951-025-03467-y.

Supplementary Material 1

Acknowledgements
Thanks to Haiyan Yu, Xiaomin Zhao, Yuyu Guo and Sen Wang from the Core Facilities for Life and Environmental Sciences at the SKLMT (State Key Laboratory of Microbial Technology, Shandong University) for the assistance provided in laser scanning confocal microscopy imaging.

Author contributions
Y. W.: Data curation, Formal analysis, Methodology, Validation, Writing-Original draft preparation. Y. S.: Data curation, Formal analysis, Validation. M. L.: Conceptualization, Investigation. C. W.: Data curation, Methodology. M. H.: Data curation, Methodology. J. Q.: Data curation, Investigation. N. Y.: Software. Y. Z.: Supervision. H. L.: Supervision. L. H.: Conceptualization, Funding acquisition, Methodology, Supervision, Writing- Reviewing and Editing.

Funding
This work was supported by the National Key R&D Plan of China (grant no. 2023YFB3210400), Open Project from the National Key Laboratory of Industrial Control Technology (ICT2024B17), the National Natural Science Foundation of China (Grant No. 32001018), the Key Research and Development Program of Shandong Province (2022CXGC020501, 2021CXGC010603), the Future Industries Cultivate Project-2022 Emerging Industries Cultivate Plan of Qingdao (22-3-4-xxgg-2-nsh), and the Shandong University Foundation for Future Scholar Plan.

Data availability
The data that support the findings of this study are available from the corresponding author upon reasonable request.

Declarations

Ethics approval and consent to participate
Not applicable.

Consent for publication
All authors have approved the manuscript and agree to the submission.

Competing interests
The authors declare no competing interests.

Author details
[1]Institute of Marine Science and Technology, Shandong University, Tsingdao 266237, P. R. China
[2]State Key Laboratory of Crystal Materials, Shandong University, Jinan 250100, P. R. China
[3]Shandong Engineering Research Center of Biomarker and Artificial Intelligence Application, Jinan 250100, P. R. China

Received: 3 March 2025 / Accepted: 14 May 2025
Published online: 03 June 2025

References

1. Havel JJ, Chowell D, Chan TA. The evolving landscape of biomarkers for checkpoint inhibitor immunotherapy. Nat Rev Cancer. 2019;19:133–50.
2. Park YJ, Kuen DS, Chung Y. Future prospects of immune checkpoint Blockade in cancer: from response prediction to overcoming resistance. Exp Mol Med. 2018;50:109.
3. Chen L, Diao L, Yang Y, Yi X, Rodriguez BL, Li Y, et al. CD38-mediated immunosuppression as a mechanism of tumor cell escape from PD-1/PD-l1 Blockade. Cancer Discov. 2018;8:1156–75.
4. Holderried TAW, De Vos L, Bawden EG, Vogt TJ, Dietrich J, Zarbl R, et al. Molecular and immune correlates of TIM-3 (HAVCR2) and galectin 9 (LGALS9) mRNA expression and DNA methylation in melanoma. Clin Epigenetics. 2019;11:161.
5. House IG, Savas P, Lai J, Chen AXY, Oliver AJ, Teo ZL, et al. Macrophage-derived CXCL9 and CXCL10 are required for antitumor immune responses following immune checkpoint Blockade. Clin Cancer Res. 2020;26:487–504.
6. Darvin P, Toor SM, Sasidharan Nair V, Elkord E. Immune checkpoint inhibitors: recent progress and potential biomarkers. Exp Mol Med. 2018;50:165.
7. Gibney GT, Weiner LM, Atkins MB. Predictive biomarkers for checkpoint inhibitor-based immunotherapy. Lancet Oncol. 2016;17:e542–51.
8. Kalluri R, McAndrews KM. The role of extracellular vesicles in cancer. Cell. 2023;186:1610–26.
9. Chang WH, Cerione RA, Antonyak MA. Extracellular vesicles and their roles in Cancer progression. Methods Mol Biol. 2021;2174:143–70.
10. Xu R, Rai A, Chen M, Suwakulsiri W, Greening DW, Simpson RJ. Extracellular vesicles in cancer — implications for future improvements in cancer care. Nat Rev Clin Oncol. 2018;15:617–38.
11. Maus RLG, Jakub JW, Nevala WK, Christensen TA, Noble-Orcutt K, Sachs Z, et al. Human melanoma-derived extracellular vesicles regulate dendritic cell maturation. Front Immunol. 2017;8:358.
12. Cordonnier M, Nardin C, Chanteloup G, Derangere V, Algros MP, Arnould L, et al. Tracking the evolution of Circulating exosomal-PD-L1 to monitor melanoma patients. J Extracell Vesicles. 2020;9:1710899.
13. Theodoraki MN, Yerneni SS, Hoffmann TK, Gooding WE, Whiteside TL. Clinical significance of PD-L1 Þ exosomes in plasma of head and neck cancer patients. Clin Cancer Res. 2018;24:896–905.
14. Theodoraki MN, Yerneni S, Gooding WE, Ohr J, Clump DA, Bauman JE, et al. Circulating exosomes measure responses to therapy in head and neck cancer patients treated with cetuximab, Ipilimumab, and IMRT. Oncoimmunology. 2019;8:e1593805.
15. Kalluri R, LeBleu VS. The biology, function, and biomedical applications of exosomes. Science. 2020;367:eaau6977.
16. Chen G, Huang AC, Zhang W, Zhang G, Wu M, Xu W, et al. Exosomal PD-L1 contributes to immunosuppression and is associated with anti-PD-1 response. Nature. 2018;560:382–6.
17. Poggio M, Hu T, Pai CC, Chu B, Belair CD, Chang A, et al. Suppression of Exosomal PD-L1 induces systemic Anti-tumor immunity and memory. Cell. 2019;177:414–27.
18. Mittelbrunn M, Gutiérrez-Vázquez C, Villarroya-Beltri C, González S, Sánchez-Cabo F, González MÁ, et al. Unidirectional transfer of microRNA-loaded exosomes from T cells to antigen-presenting cells. Nat Commun. 2011;2:282.
19. Sung BH, von Lersner A, Guerrero J, Krystofiak ES, Inman D, Pelletier R, et al. A live cell reporter of exosome secretion and uptake reveals pathfinding behavior of migrating cells. Nat Commun. 2020;11:2092.
20. Sposini S, Rosendale M, Claverie L, Van TNN, Jullié D, Perrais D. Imaging endocytic vesicle formation at high Spatial and Temporal resolutions with the pulsed-pH protocol. Nat Protoc. 2020;15:3088–104.
21. Bonsergent E, Grisard E, Buchrieser J, Schwartz O, Théry C, Lavieu G. Quantitative characterization of extracellular vesicle uptake and content delivery within mammalian cells. Nat Commun. 2021;12:1864.
22. Mathieu M, Névo N, Jouve M, Valenzuela JI, Maurin M, Verweij FJ, et al. Specificities of exosome versus small ectosome secretion revealed by live intracellular tracking of CD63 and CD9. Nat Commun. 2021;12:4389.
23. Ji Y, Qi D, Li L, Su H, Li X, Luo Y, et al. Multiplexed profiling of single-cell extracellular vesicles secretion. Proc Natl Acad Sci U S A. 2019;116:5979–84.
24. Song F, Wang C, Wang C, Wang J, Wu Y, Wang Y, et al. Multi-Phenotypic exosome secretion profiling microfluidic platform for exploring Single-Cell heterogeneity. Small Methods. 2022;6:2200717.
25. Li L, Su H, Ji Y, Zhu F, Deng J, Bai X, et al. Deciphering Cell–Cell interactions with integrative Single-Cell secretion profiling. Adv Sci. 2023;10:2301018.
26. Wang C, Zhang Y, Wang J, Han Y, Wang Y, Sun M et al. Single-Cell isolation chip integrated with multicolor barcode array for High-Throughput Single-Cell exosome profiling in tissue samples. Adv Mater. 2024;2411259.
27. Teng MWL, Ngiow SF, Ribas A, Smyth MJ. Classifying cancers basedon T-cell infiltration and PD-L1. Cancer Res. 2015;75:2139–45.
28. Sabhachandani P, Motwani V, Cohen N, Sarkar S, Torchilin V, Konry T. Generation and functional assessment of 3D multicellular spheroids in droplet based microfluidics platform. Lab Chip. 2016;16:497–505.
29. Sun Q, Tan SH, Chen Q, Ran R, Hui Y, Chen D, et al. Microfluidic formation of coculture tumor spheroids with stromal cells as a novel 3D tumor model for drug testing. ACS Biomater Sci Eng. 2018;4:4425–33.
30. Alessandri K, Sarangi BR, Gurchenkov VV, Sinha B, Kießling TR, Fetler L, et al. Cellular capsules as a tool for multicellular spheroid production and for investigating the mechanics of tumor progression in vitro. Proc Natl Acad Sci U S A. 2013;110:14843–8.
31. Grist SM, Nasseri SS, Laplatine L, Schmok JC, Yao D, Hua J, et al. Long-term monitoring in a microfluidic system to study tumour spheroid response to chronic and cycling hypoxia. Sci Rep. 2019;9:17782.

32. Tomasi RFX, Sart S, Champetier T, Baroud CN. Individual control and quantification of 3D spheroids in a High-Density microfluidic droplet array. Cell Rep. 2020;31:107670.
33. Yu L, Chen MCW, Cheung KC. Droplet-based microfluidic system for multicellular tumor spheroid formation and anticancer drug testing. Lab Chip. 2010;10:2424–32.
34. Wang Y, Wang J. Mixed hydrogel bead-based tumor spheroid formation and anticancer drug testing. Analyst. 2014;139:2449–58.
35. Lee JM, Choi JW, Ahrberg CD, Choi HW, Ha JH, Mun SG, et al. Generation of tumor spheroids using a droplet-based microfluidic device for photothermal therapy. Microsystems Nanoeng. 2020;6:52.
36. Saint-Sardos A, Sart S, Lippera K, Brient-Litzler E, Michelin S, Amselem G, et al. High-Throughput measurements of Intra-Cellular and secreted cytokine from single spheroids using anchored microfluidic droplets. Small. 2020;16:2002303.
37. Jiang X, Ren L, Tebon P, Wang C, Zhou X, Qu M, et al. Cancer-on-a-Chip for modeling immune checkpoint inhibitor and tumor interactions. Small. 2021;17:2004282.
38. Liu M, Wang Y, Wang C, Li P, Qiu J, Yang N, et al. A microfluidic 3D-Tumor-Spheroid model for the evaluation of targeted therapies from Angiogenesis-Related cytokines at the single spheroid level. Adv Healthc Mater. 2024;13:2402321.
39. Prince E, Kheiri S, Wang Y, Xu F, Cruickshank J, Topolskaia V, et al. Microfluidic arrays of breast tumor spheroids for drug screening and personalized Cancer therapies. Adv Healthc Mater. 2022;11:2101085.
40. Thorsson V, Gibbs DL, Brown SD, Wolf D, Bortone DS, Ou Yang TH, et al. The immune landscape of Cancer. Immunity. 2018;48:812–30.
41. Wang ZJ, Farooq AS, Chen YJ, Bhargava A, Xu AM, Thomson MW. Identifying perturbations that boost T-cell infiltration into tumours via counterfactual learning of their Spatial proteomic profiles. Nat Biomed Eng. 2025;9:390–404.
42. Zheng L, Qin S, Si W, Wang A, Xing B, Gao R, et al. Pan-cancer single-cell landscape of tumor-infiltrating T cells. Science. 2021;374:eabe6474.
43. Qiu Y, Yang Y, Yang R, Liu C, Hsu JM, Jiang Z, et al. Activated T cell-derived Exosomal PD-1 attenuates PD-L1-induced immune dysfunction in triple-negative breast cancer. Oncogene. 2021;40:4992–5001.
44. Yang Y, Li CW, Chan LC, Wei Y, Hsu JM, Xia W, et al. Exosomal PD-L1 harbors active defense function to suppress t cell killing of breast cancer cells and promote tumor growth. Cell Res. 2018;28:862–4.
45. Chow A, Zhou W, Liu L, Fong MY, Champer J, Van Haute D, et al. Macrophage Immunomodulation by breast cancer-derived exosomes requires Toll-like receptor 2-mediated activation of NF-κ B. Sci Rep. 2014;4:5750.
46. Petrova YI, Schecterson L, Gumbiner BM. Roles for E-cadherin cell surface regulation in cancer. Mol Biol Cell. 2016;27:3233–44.
47. Van Roy F, Berx G. The cell-cell adhesion molecule E-cadherin. Cell Mol Life Sci. 2008;65:3756–88.
48. Wang L, Zhu J, Shan S, Qin Y, Kong Y, Liu J, et al. Repression of interferon-γ expression in T cells by Prospero-related homeobox protein. Cell Res. 2008;18:911–20.
49. Hayashi K, Ishizuka S, Yokoyama C, Hatae T. Attenuation of interferon-γ mRNA expression in activated Jurkat T cells by exogenous zinc via down-regulation of the calcium-independent PKC-AP-1 signaling pathway. Life Sci. 2008;83:6–11.
50. Wang C, Zhang Y, Tang W, Wang C, Han Y, Qiang L, et al. Ultrasensitive, high-throughput and multiple cancer biomarkers simultaneous detection in serum based on graphene oxide quantum Dots integrated microfluidic biosensing platform. Anal Chim Acta. 2021;1178:338791.
51. Wang C, Wang C, Qiu J, Gao J, Liu H, Zhang Y, et al. Ultrasensitive, high-throughput, and rapid simultaneous detection of SARS-CoV-2 antigens and IgG/IgM antibodies within 10 min through an immunoassay biochip. Microchim Acta. 2021;188:262.
52. Wang C, Wang C, Wu Y, Gao J, Han Y, Chu Y, et al. High-Throughput, living Single-Cell, multiple secreted biomarker profiling using microfluidic chip and machine learning for tumor cell classification. Adv Healthc Mater. 2022;11:2102800.
53. Möller A, Lobb RJ. The evolving translational potential of small extracellular vesicles in cancer. Nat Rev Cancer. 2020;20:697–709.

Publisher's note